

Anthropogenic change detection on and close to the Moon for space domain awareness

David P. Osterman, Jeffrey E. Van Cleve, Anna Lawitzke, Jacob D. Griesbach,
Christopher J. Grant, Colleen Olson
Ball Aerospace, Colorado

ABSTRACT

We live in a moment of history when we would like to be aware of events on and near the lunar surface, though whether such awareness falls within the scope of Space Domain Awareness (SDA) – because the Moon is a body in space, as considered by Earthlings – or whether it is more akin to GEOINT, since the Moon is a geographical area from the perspective of those who operate on its surface, is a matter of some controversy. Reworking the definition of GEOINT for the Moon, we consider lunar surface intelligence (LUNINT). LUNINT includes objects landing on or operating on the surface, their disturbances of the natural surface (tracks, excavation or burial, impact craters) and their emissions of dust, gas, and RF, as well as vehicles transiting from one surface location to another by means of surface traction or suborbital propulsive means. LUNINT is more difficult than GEOINT in the sense that non-polar locations are subject to 14-day night gaps in optical visibility, but easier than GEOINT in the sense that the Moon is easy to model compared to the Earth (hence changes are easier to detect against clutter) and does not suffer weather outages. In this paper, we discuss NASA’s Lunar Reconnaissance Orbiter (LRO) [1], a science and exploration mission which demonstrates detection of anthropogenic features such as the Apollo and Chang’e landers and rovers [2] with 0.5 m pixels. For future missions, we consider observations from an LRO-like low circular polar orbit, an elliptical orbit as discussed in a companion paper [3], and a sun-synchronous lunar orbit. The observations include electro-optical (EO) and IR cameras observing the directly illuminated surface of the Moon, as well as observing the permanently-shadowed interiors of lunar craters which can be imaged in scattered light from crater rims or the thermal emission from the absorption of that scattered light in the crater. We present an analytic model of the illumination of crater interiors based on [4] and an STK model which renders scenes using LRO digital elevation maps (DEMs). We derive SNR, ground sampling distance (GSD), and contrast requirements for VIS/NIR sensors in orbit around the Moon, which we relate to the National Imagery Interpretability Scale (NIIRS) familiar to the GEOINT community [5]. An enhanced payload suite may include non-photon sensors for detection of vehicle landing and takeoff by spectroscopic detection of H₂O from lander plumes [6, 7], and dust counter detection of plume dust ejecta flung into orbit-crossing paths [8]. These capabilities also have science applications such as topographic mapping, mineralogy, detecting flashes from meteor impacts [9, 10] and fresh craters [11, 12], and volatile detection.

1 Introduction: Exploration of Cislunar Mission Space

1.1 Overview of the Cislunar Domain

While SDA has historically been practiced in the LEO to GEO domains, the growing quantity of missions and traffic to cislunar space drives the importance and need for above-GEO (XGEO) SDA. As an example, NASA’s ARTEMIS and Commercial Lunar Payload Services (CLPS) programs, AFRL’s CHPS, and the future planned Chinese activities will lead to numerous assets and rocket bodies launched into the Earth-Moon gravitational corridor in the coming years. Cislunar SDA systems will be critical to protecting and maintaining operational confidence for safe transit.

XGEO distances are generally an order-of-magnitude beyond those typically implemented for GEO sensing, driving the need for high-performance, long-range optical systems. The same sensors that may be adequate for proliferated LEO satellite systems will be insufficient to monitor the vastness of XGEO space. Even cislunar space traffic management (STM) requires a higher sensitivity optical system than SDA in GEO due to the long ranges, larger search volumes, and complex cislunar orbits. Observability in the cislunar corridor is also challenging and limited due to lunar, earth, and solar angular exclusion zones. Because of this, one or more low lunar orbiters are required to completely cover the 4π steradian cislunar regime by tracking low lunar orbit satellites and their sources and sinks on the lunar surface.

1.2 Why Look Down at the Moon?

In the context of the broad cislunar space discussed above, we propose observations of the lunar surface from orbits which at least at periapsis pass close enough to the surface to detect and resolve meter-size objects, for several reasons. First, the lunar surface and near-Moon space is a boundary of cislunar space. Cislunar SDA then includes tracking objects as they enter or leave low orbits around the moon, or land and take off from the lunar surface, to account for

objects throughout their life cycle. Second, the lunar surface and near-Moon space are very difficult to observe from the ground, or even from sensors in geosynchronous or Earth-Moon Lagrange point stations, because of lunar straylight, surface clutter for transiting targets, and invisibility of occulted targets. Third, we expect various parties to have high-value assets on the lunar surface. This paper is related to these companion papers at this conference which explore other aspects of cislunar SDA:

- Joint SDA-LUNINT mission which combines limited awareness of the surface with Lagrange-zone SDA in a single sensor [3]
- Awareness of near-Moon space and the interior of Shackleton Crater from sites on the lunar surface [13] which complements the awareness of the surface as seen from space discussed in this paper
- Architecture optimization for SDA of the volume above 3x GEO and along the Earth-Moon transfer corridor from sensor constellations located in a variety of 3-body and geocentric orbits [14]

2 Mission Architecture Elements

2.1 Bounding-Case Orbits

Missions like LRO which have as their goal global, high-resolution imagery are in Polar Circular Low Lunar Orbits (PCLLOs). In a sweet spot between 50 and 100 km altitude [15, 16], the orbit is weakly perturbed by 3rd body (Earth and Sun) potentials, while the altitude is high enough to avoid heavy perturbation by mascons and resultant maintenance Δv costs. Below 50 km, perturbative forces increase as the inverse cube of altitude (simplifying mascons as dipole gravity fields) while above 50 km one has to shrink the IFOV (and hence camera FOV, for the same pixel count) to maintain desirable GSD. Thus a 50 km PCLLO was chosen for LRO's one-year primary mission, though LRO maneuvered to 20 km x 165 km frozen orbit [15] for high-resolution mapping of the Lunar South Pole, which conserved fuel despite the low perapsis. LRO carried enough fuel to have 450 m/s Δv for maneuvers and maintenance after orbit insertion [1] and is still operating after 13 years.

A polar eccentric lunar orbit (PELO) is useful to reduce maintenance Δv costs for low-periapsis orbits and perform another mission when further from the Moon where the apparent disk of the Moon subtends less of the sky (for SDA) or where the vehicle is moving slowly (for communication and RF monitoring of the surface). For the Hybrid SDA-LUNINT mission presented in detail in [3], a hybrid 30 x 750 km orbit was found to be least sub-optimal for the joint SDA-LUNINT mission. Eccentricity may also be useful for frozen orbits [16] which have much lower orbit maintenance requirements than arbitrary combinations of orbital elements constrained to the same periapsis altitude and location on the lunar surface. For example, [15] discusses a frozen 43 x 204 km orbit ($e = 0.043$) with its periapsis over the South Pole.

The Sun-synchronous lunar orbit was discussed in [17], who found that while a low-latitude ($<30^\circ$) sun-synch orbit driven by the small lunar J_2 was possible, a truly sun-synchronous orbit covering the poles was not possible using only the lunar gravity field. It is conjectured, but not shown here, that Earth and Sun perturbations might make a polar sun-synch orbit possible, since close polar orbits are inertial and NRHO orbits rotate at the synodic rate, so maybe in between there is an orbit which rotates 1°/day.

2.2 Electro-Optic and Infrared Imagery

This section describes some basic principles of EOIR surface imagery applied to the surface of the Moon, rather than instrument designs. We consider directly illuminated surfaces, scattered light, and thermal emission.

The directly Sun-illuminated Moon is bright by astronomical standards, both in reflected visible light and thermal emission, but since we are interested in imaging the permanently-shadowed regions (PSRs) in crater interiors using direct Earthshine and by light scattered from crater rims we show some radiometry here and in the next section. The signal for direct incidence on a surface is:

S_0 = solar constant in band in W/m²

a = albedo

h = altitude of sensor at a given point in its orbit

ϕ = IFOV = FOV/# of pixels; solid angle $\Omega_{pix} = \phi^2$. GSD = $h\phi$ (see 2.2.4 for GSD)

F = F-number of camera, of aperture D

f = focal length of camera = FD

Ω_{pix} = solid angle of incoming radiation seen by pixel = $\pi/4F^2$

$x = \text{pixel pitch} = \phi f = \phi DF$

$e_0 = \text{solar elevation angle relative to geoid. The minimum summer solstice } e_0 \text{ is the inclination of the lunar equator to the ecliptic, } 1.54 \text{ degrees}$

Surface radiance = $aS_0 \sin e_0 / \pi \text{ Wm}^{-2}\text{sr}^{-1}$

Power scattered into camera pixel = $(aS_0/\pi) \Omega_{\text{pix}} x^2 \sin e_0 = aD^2 \phi^2 S_0 \sin e_0 / 4$

SNR of a pixel is then calculated from the FPA properties, the integration time per read (typically the orbital velocity/GSD), and the number of reads averaged per output pixel.

For thermal radiometry, the surface temperature can be estimated from thermal models and LRO DIVINER thermal imaging data [18]. The instrument can be a room-temperature bolometer or thermopile, which has relatively low sensitivity but simple thermal requirements, or a more ambitious photon-counting detector such as HgCdTe, which may have to be cooled to as low as 50 K depending on the cutoff wavelength desired.

The PSRs are among the most interesting places on the Moon, as they are expected to contain water ice and other volatiles which will be scientifically interesting and contain important resources for future explorers for life support and propellant. They were studied by LRO in scattered visible light, UV starlight, and infrared emission [1]. The lunar south polar region and PSRs are the target of several international lander missions in the next years including NASA's VIPER, PRIME-1, and CLPS-5 (carrying the Ball-built thermal imaging camera L-CIRiS) and China's Chang'e 6 and 7 and of a multitude of orbiters and technology demonstration missions. Hence, it may be of some interest to observe activity in the PSRs and calculate the illumination levels in PSRs for visible and IR light. This calculation is also applicable to shadows inside non-polar craters near the lunar terminator.

Following [4] and some notation changes to avoid confusion with camera parameters D , F , and f (see Fig. 2-1)

$d = \text{crater depth}$

$r_c = \text{crater radius in the horizontal plane of the crater rim}$

$w = \text{diameter-to-depth ratio} = 2r_c/d$. Typically 5-10 [19]

$r = \text{radius of sphere, of which the physical crater is the lower cap} = wd/2\beta = w^2d/8$.

$\beta = \text{half-angle of crater} = 4/w$

$g = \text{ratio of surface area of the inside of the crater to the inside of the sphere} = 4/w^2$

– that is, a crater exactly at a pole at summer solstice.

The total single-scattered power inside the crater is then $agS_0(\sin e_0)\pi d^2 w^2/4$. The spherical area of the crater is $\pi d^2 w^2/4$ so the flux to lowest order in $1/w$ is $4aS_0(\sin e_0)/w^2$ and substituting this expression for S_0 in the direct imaging equation we get that the power scattered into the camera is $a^2 D^2 \phi^2 S_0(\sin e_0)/w^2$. The flux ratio between a rock normal to the Sun and camera and the shadow is then $w^2/4a(\sin e_0)$, which we can take as the dynamic range requirement for the camera = 10^4 for $w = 10$ and $e_0 = 1.5^\circ$. Following [19] we then take the $1/4$ power of the flux in the shadow to estimate the insolation temperature of the PSR as about 10% of that of the noontime surface or ~ 41 K. The shadowed parts of shallower craters are darker and colder since the surface in the shadow sees a smaller sliver of reflected light from the crater rim. While it is obvious from these equations that the crater interior will be exceedingly dark and cold in the southern winter (that is, $e_0 < 0$), the PSR will be of continuing LUNINT interest for observing infrastructure and vehicles parked on the peaks of persistent light [13] and for observing thermal emissions from equipment operating in the PSR. Indeed, DIVINER thermal data [18, 20] show that the surface is cold (down to ~ 40 K) but measurable even in the winter near the poles.

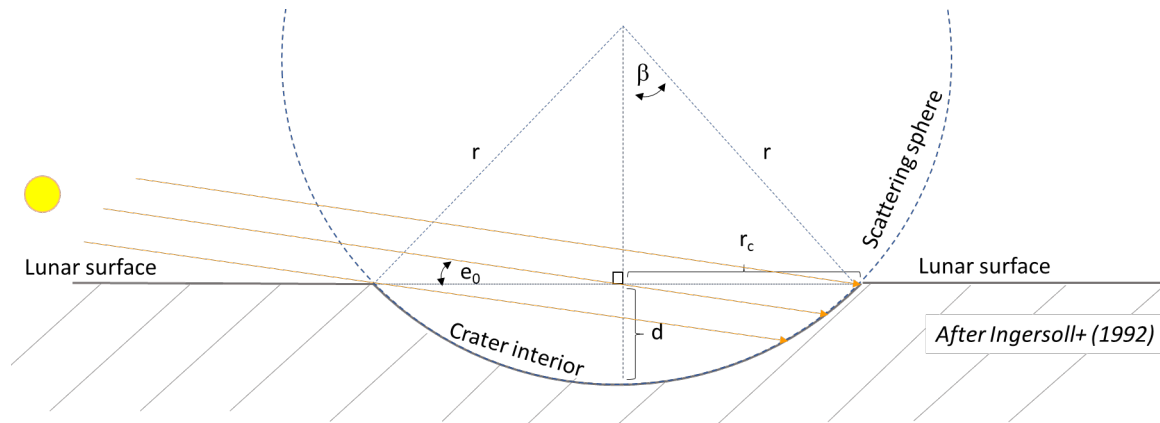


Fig. 2-1: Spherical Bowl-Shaped Crater Radiometry, after Ingersoll+ (1992)

As examples, LRO-LROC images of Shackleton can be browsed with Quickmap (<https://quickmap.lroc.asu.edu>) and LRO-DIVINER temperature maps of the S. Polar regions can be found in [18] and the DIVINER data page <https://www.diviner.ucla.edu/data>.

Earthshine is about 10^{-4} as bright as the Sun and dominates starlight by several orders of magnitude during the lunar night [21]. Happily, this is about the same ratio as typical illumination of PSRs by scattered rim light and direct illumination (§2.2.2), so a camera capable of imaging PSRs from orbit can perform useful imaging in direct Earthshine. Earthshine is useful for Nearside poles since Earth can be 6° above the geoid horizon once a month while max solar elevation is 1.5° with up to a 6 month period of darkness in the winter [21]. The LPI South Pole Atlas contains an Earthshine mean intensity map with 5° of the pole [22], showing that the North slope of Malapert is particularly well-illuminated by Earthshine for much of the month.

2.3 Image Quality: GSD and NIIRS

Fig. 2-2 shows that a GSD of 0.5 m/pix shows awareness of the activities and objects associated with Apollo 15, while at 2.0 m/pix some evidence of activity is seen but without much insight to the objects and activities. The images are from Quickmap and the location of anthropogenic features is described in [2]. Hence, we will take a GSD of 0.5 m/pix for missions doing only LUNINT and relax it somewhat to 0.5-2.0 m/pix for hybrid SDA missions. The 0.5 m pixel then determines 10 μ rad IFOV for a 50 km orbit and a 3.4 kHz readout rate for a 1.70 km/s orbital velocity.

While the General Image Quality Equation (GIQE) used to estimate NIIRS includes GSD, SNR, optical image quality, and image sharpening algorithms, in the limit of sharp images and high SNR (>10) NIIRS increases by 1 for each factor of 2 decrease in GSD [5]. The literature often notes GSD in inches for historical reasons, in which case the GIQE is approximately $NIIRS = 10.3 - \log_2(GSD/inch)$. The 2.0 to 0.5 m GSD then corresponds to $NIIRS = 4$ to 6, respectively. The corresponding verbal descriptions are “Identify tracked vehicles by general type” and “Identify automobiles as sedans or station wagons,” in rough agreement with Fig. 2-2. The predictability of the Moon’s surface illumination (§3.2) allows inclusion of the SNR term in the NIIRS GIQE for more detailed future work.

While DIVINER has written the current textbook about lunar surface thermal properties, DIVINER’s 3.6 mrad IFOV projects to a GSD of 180 m from an altitude of 50 km, so at least an order of magnitude smaller thermal GSD would be needed for useful LUNINT at these wavelengths. In a similar vein, Hayne+ [23] look for microtraps much smaller than the DIVINER pixel, in which water can be frozen.

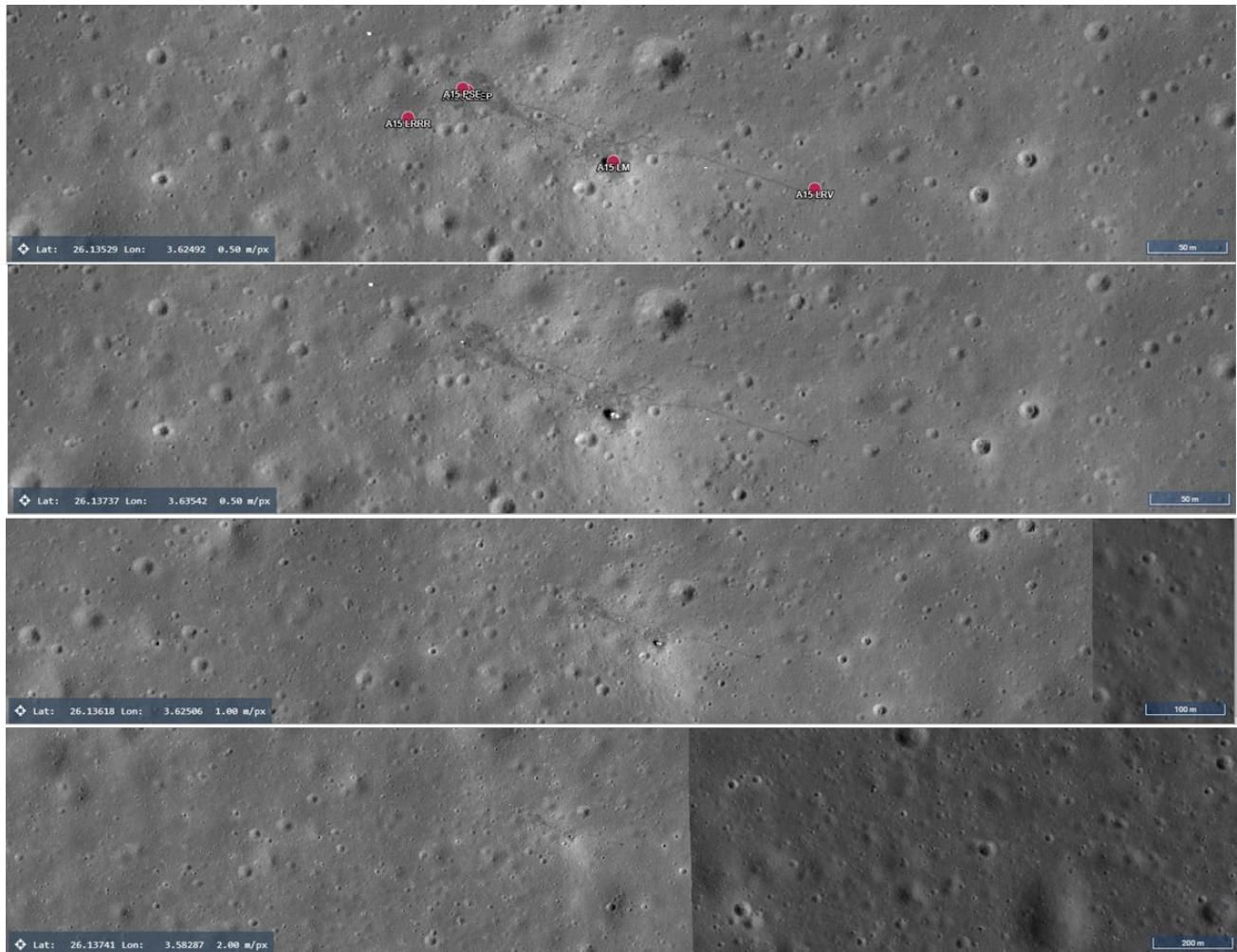


Fig. 2-2: Apollo 15 landing site at various GSDs. The scale and resolution are at the bottom of each subpanel. The top panel overlays labels for anthropogenic features. Note foot and moon buggy trails. Credit: NASA/ASU/Quickmap.

2.4 Cross-Track FOV

For each orbit of a PCLLO, the Moon rotates inertially by 16.6 km/hr or about 30 km/orbit. To seamlessly image on the subsequent orbit then requires a rather large cross-track FOV (33°) from 50 km and corresponds to 60,000 cross-track 0.5 m pixels – an unwieldy number! PCLLO missions thus carefully trim their altitudes so that the ground track on subsequent months passes one FOV away from the previous month's, so global coverage is built up over a year. This is a rather long latency for LUNINT, so a constellation of PCLLOs will be needed for timely global coverage in the future if that becomes required.

However, in the short term the locus of human activity appears to be within 5° of the South Pole. Since the inertial ground track shifts by 2.6 km at 85S, corresponding to an XT FOV of 3.0° and 5200 XT pixels, an imager like LRO's LROC-NAC with 5064 XT pixels can completely image the polar cap every two weeks.

2.5 EOIR Observing Calendar

A fundamental feature of observing the lunar surface from LLO, in which the orbit plane may be approximated as inertially fixed, is that one must wait for a specific solar elevation angle during overflight for 3 to 6 months while the Sun-to-orbit plane angle changes seasonally and choose the right orbit of the month to actually overfly the target. Polar revisit times, of course, diminish in proportion to the cosine of latitude. Fig. 2-3 shows the illumination of the Moon and the inertial orbit as seen from the Earth for the first year of the mission. Since the orbit is inertial, a natural way of presenting the calendar is by quarters of a sidereal month (horizontal) and by sidereal months (vertical axis).

The orbit is shown as a green circle, with the ascending node indicated by a triangle. If the ascending node is not visible from the Earth, the descending node is indicated by an inverted triangle. The quarter-month intervals emphasize Earth-viewing geometry changes, while the solar illumination at nadir remains roughly constant. The month intervals emphasize Sun-viewing changes, while the Earth-viewing geometry remains roughly constant. The rows of the calendar are spaced in 3 or 4 sidereal months to show the Sun-viewing changes over rough quarters of a calendar year. The spacing of the calendar in sidereal months is not in equal intervals, since there are roughly 13.4 sidereal months in a calendar year, while holding the Earth-viewing geometry constant in the horizontal series requires beginning each row with the same sidereal quarter.

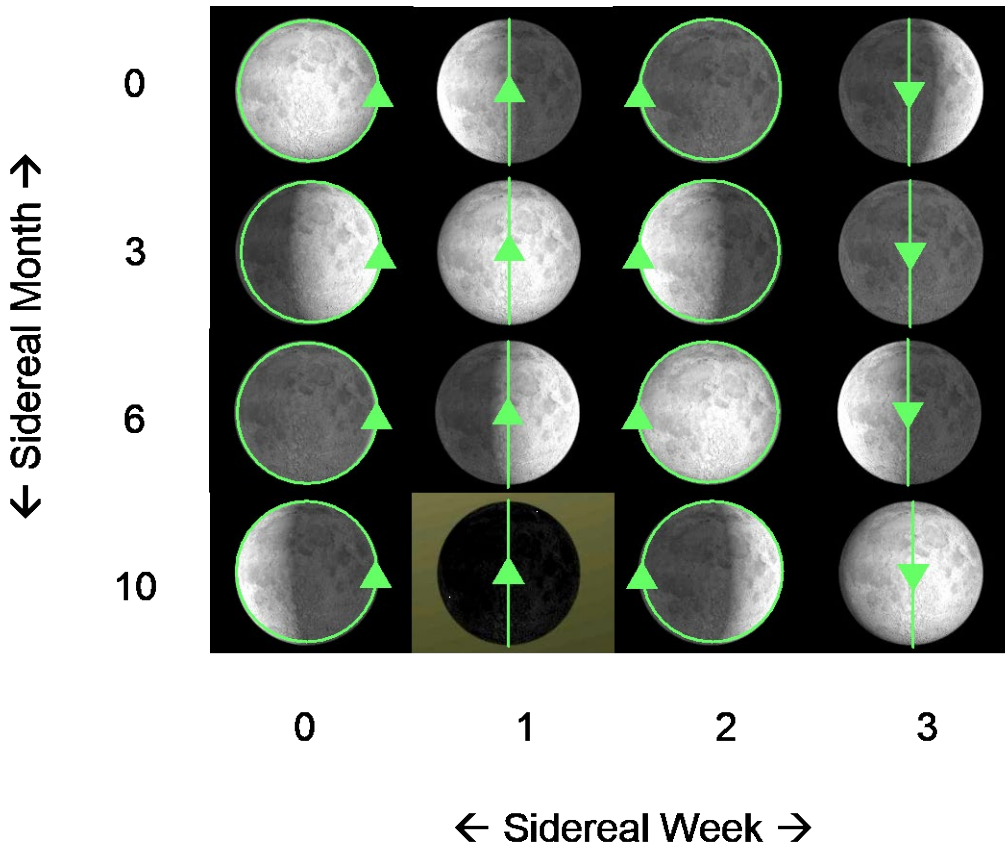


Fig. 2-3: Visual Lunar Observing Calendar

Fig. 2-3 is an equator-centered view of the Moon. While the diurnal illumination in the polar regions is strongly topography-dependent, the overall illumination level will be set by the seasons, as shown in Table 2-1.

Table 2-1: Lunar Seasons for a Near-Term Mission

Date	JD	MET (d)	Subsolar			
			Longitude	Latitude	N	S
2025-Mar-17	2460751.5	0	329.9	-0.01	Spring	Fall
2025-Jun-11	2460837.5	86	0.3	1.58	Summer	Winter
2025-Sep-11	2460929.5	178	316.4	-0.01	Fall	Spring
2025-Dec-15	2461024.5	273	239.4	-1.53	Winter	Summer
2026-Feb-26	2461097.5	346	71.4	-0.06	Spring	Fall

3 Finding Changes in Lunar Images

3.1 Compare Before and After Images

The LRO-LROC team discovered a double crater near Hertzsprung crater (5.2°N, 234°E) on the lunar Farside from a rocket body crash [24], which was conjectured but not proven to be from Chang’e 5 T1. Unlike the Apollo S-IVB craters, imagery was collected before and after the event was collected. As noted in the corresponding *New York Times* story [25], “Usually, a computer program does the comparison, but that works best if the before-and-after pictures are taken at the same time of day. For this search, many of the images were taken at different times, and difference in shadows confused the algorithm.” A tedious manual search ensued.

3.2 Modeling the “Before” Lunar Surface Image

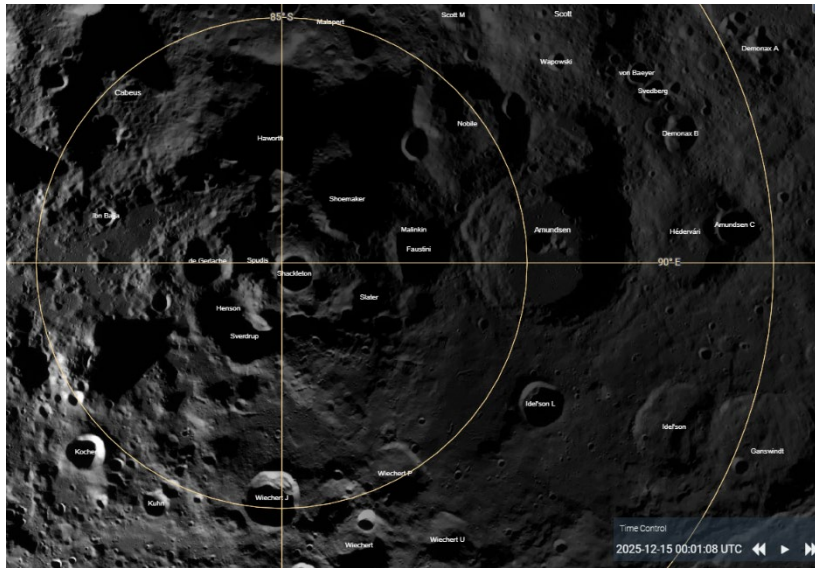


Fig. 3-1: S. Pole illumination from Quickmap

control banner pops up with the current time. Time can then be entered directly for the circumstances of interest. An example is shown in Fig. 3-1.

Another method for synthesizing images of the lunar surface employs STK, a commercially available software tool, and terrain data from prior lunar missions imported from the NASA PDS (Planetary Data System). This method forms the basis of an ongoing effort to validate the illumination results of the prior sections with an alternative calculational approach utilizing STK’s spatial and temporal modeling capabilities. When the STK and LRO LROC imagery have been cross-validated, we will use STK for end-to-end mission planning for observing the lunar surface. A series of example STK images of the proposed Shackleton SDA station sites 1 and 2 [13] as seen from above at various times of the lunar day are shown below, from the same observer position. We are thus able to coordinate links between assets in orbit and on the surface, while continuing to investigate the photometric accuracy of these images.

For an operational LUNINT system, one would want to model the “before” scene using existing imagery and DEMs. Unlike the Earth, the Moon lacks weather and seasonal vegetation, so it is possible to model the “before” scene to higher fidelity for the Moon. Mazarico+ [26] present an advanced illumination model of the Moon (IllumNG), which generalizes our simple discussion of double scattering inside bowl-shaped craters (§2.2.2) and Earthshine (§2.2.3) to the actual topography, using data from the LRO LROC camera and LOLA altimeter.

Quickmap users can get qualitative illumination images by selecting the desired map projection, then “Sunlit Region” under “Overlays.” A time

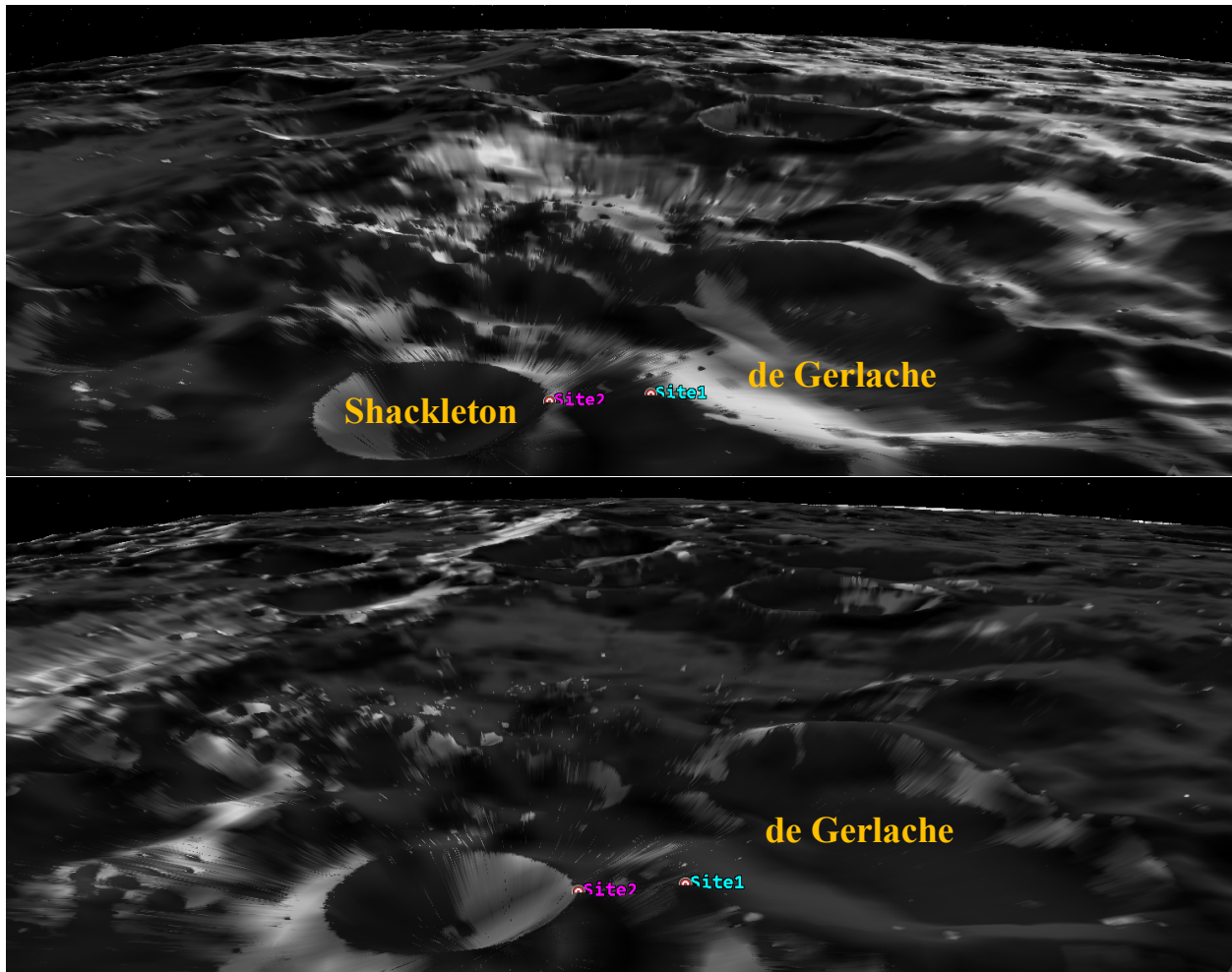


Fig. 3-2: STK renderings of region near S. Pole showing lunar surface SDA sites [13] seen from above. Top: 23 May 2025 19:24:44 Bottom: 5 Jun 2025 11:42:25

3.3 Target EOIR Modeling

We expect that the modeling of space hardware of the lunar surface will be as complicated as the detailed modeling of space objects, including an inventory of surface element geometry and materials and their associated scattering functions. Such detailed simulations are available from others. To convey ideas simply, we model the surface target as a 1.0 m Lambertian sphere of 20% albedo. This will be Nyquist-resolved at the recommended nadir GSD and will have high contrast against the 10% albedo median lunar surface. Future work could include modeling shadows, and contrast against the brighter (highlands) soils of the Moon.

The lander rocket exhaust “blast zone” (BZ) is composed of a regions of lower soil reflectance that extends a few meters out from the lander and a larger high reflectivity halo out to a few hundred meters away [27]. Larger landers have larger BZs, and the data on Surveyor, Luna, and Apollo suggest that the area of the blast zone is roughly proportional to the mass of the lander ([27] Table 2) and hence the mass of propellant expelled during final approach and landing. Hence, the area of the BZ may be used to roughly infer the mass of the lander when the lander itself is unresolved in imagery. To do this, residual errors from noise and calibration systematics in the image must be smaller than the observed contrast between BZ and nearby undisturbed soils, which is typically 10% ([27] Table 2) – implying a per-pixel system radiometric accuracy of about 5%, which can in turn be partitioned into optical smear, SNR, and calibration residual terms. Reference [28] applies the methods of [27] to the 2013 Chang’e 3 BZ with additional insights from having before-landing imagery of the site for the same sensor (LRO LROC-NAC). The casual Quickmap browser can see the inner (dark) and outer (bright) BZs around Apollo landers (Fig. 2-2). Keep in mind

that the dark area to the left (west) of the lander is a shadow not an albedo feature since Apollo landed in lunar mid-morning.

The trails left by the astronauts and their “moon buggy,” as well as the trail of the Yutu rover in the Chang’e 3 images [28] are also quite noticeable. Reference [28] suggests a 5% reflectance decrease compared to the background suggesting that the image contrast limits derived for [27] are comparable. Further work needs to be done to understand how albedo change in vehicle trails depends on wheel design, vehicle mass, driving style, and regolith properties.

4 Physical Sensors

While we propose electro-optical imagery as the primary anthropogenic change detection method on an orbiter it is important to note that other detection methods could be utilized to provide additional lunar activity detection approaches. Such non-photon payloads would provide additional capability for detecting surface mining activities, lunar launches, and landings. This may be considered a form of local space awareness, in the sense that these non-photon particles are in trajectories through space, and are monitoring objects entering or leaving space via the lunar surface. It may also be considered a form of local lunar surface intelligence, in that the particles have information on activities on the lunar surface itself.

4.1 Gas

Gas from landings is detectable locally and even globally. Spacecraft exhaust volatiles typically remain in the lunar exosphere or deposit in the lunar regolith within one orbit. Results described in [7, 29] show that within 2 days ~60-70% of the water released has been photodestroyed while ~13% of the exhaust gases have made it to the polar permanently shadowed regions (PSRs) and bound to the regolith by cold traps [6, 30]. During that time, we propose using a gas chromatography–mass spectrometry (GC/MS) payload to sample the exosphere to identify exhaust volatiles. GC/MS has the benefit of combining gas chromatography with traditional mass spectrometry which is often used on Earth to identify molecular residues, drugs, and in forensics. GC/MS was used on the Cassini mission to test the atmospheric content of Saturn’s moon Titan and most recently the Neutral Gas and Ion Mass Spectrometer (NGIMIS), on the Mars Atmosphere and Volatile Evolution Mission (MAVEN) investigated the loss of atmospheric gases to space. NGIMIS had a sensitivity of 10^{-2} (counts/s)/(particles/cm³), mass range of 2-150 daltons, and a mass resolution of 1 dalton [31, 32]. This mass range and sensitivity would support globally detecting the outgassed plume material from a Chang'e 3 class lander (dry mass ~1,200 kg), which is expected to have density of 30-3000 cm⁻³ at 50 km altitude ([29] Fig. 5).

4.2 Dust

Landing – and presumably ascent – can spread small regolith grains far from the landing site, including into orbit, which may be of concern for LLO assets and even the Lunar Gateway ([8] Fig. 4). Detection of such grains will use the same technology as NASA’s LADEE-LDEX instrument [33], which was the first high-sensitivity dust counter in lunar orbit. Unlike the detection of slow-moving grains from nearby sites on the lunar surface [13] which might use a temperature-controlled quartz crystal microbalance (TQCM), the high relative motion of sensor and grain results in a hypervelocity impact may be best sensed with an ionization counter like LDEX. The LDEX detection limit for individual particles was about 1.0 μm diameter, though it also integrated subthreshold current to measure smaller particles in the aggregate. These 1.0 μm particles can have a maximum ejecta velocity in excess of lunar escape velocity [8]. The ejection geometry is in sheets between 1 and 3 degrees above the local surface, so monitoring landings at the poles would best be done from a polar orbit.

The absolute amount of dust excavated as a function of altitude and lander (and hence propellant) mass is a matter of conjecture and current research. The natural background of $> 1.0 \mu\text{m}$ grains at 50 km altitude is $\sim 2 \times 10^{-4} \text{ m}^{-3}$ ([33] Fig. 1), corresponding to a ram flux of 0.3 grains/m²/s ([33] Fig. 2) for a relative velocity equal to the LLO velocity of 1680 m/s, or 14 counts/h for a detector the size of LADEE-LDEX. For order of magnitude estimation, 20% of the regolith by volume is $< 20 \mu\text{m}$ grains [34], and a typical grain size distribution of $1/d^3$ then gives about 1% of the mass in the 1.0 μm grains that might make it into orbit. A ton of regolith excavated by ~ 5 tons of propellant then corresponds to 10^{16} grains, which if evenly distributed over the Moon to a height of 100 km gives 2.6×10^{-3} grains/m³, considerably in excess of the natural background.

5 SDA Close to the Moon from Orbit

The observation of craft in suborbital or landing/takeoff trajectories is a relatively new problem, which until this moment of history has not been of great interest since at most one such vehicle has been active at any one time. However, we expect that to change rapidly in the late 2020's as vehicles from several states and non-state actors arrive at the Moon.

5.1 Observations of Landing and Takeoff

A typical timeline for a vehicle landing on the Moon is to start from a low (50-100 km) but stable circular parking orbit, then do a small maneuver to place periapsis about 15 km above the landing site, as was done for Apollo. About 400 km short of the landing site, powered descent begins and lasts about 7 minutes [35]. The start of the burn is well over the horizon (230 km) from an observer at the landing site, so it is worth considering how well that a landing can be observed. This has two parts: First, observing the maneuver to a low perilune orbit. This gives the observer about an hour to notice the orbit change before the powered descent begins, but the actual destination along the ground track is uncertain by 100's of kilometers until the powered descent begins. Second, observing the powered descent. This is more difficult, since only 7 minutes are available (a small fraction of the observer's orbital period) and the lander will in general be close to the limb, taxing the straylight suppression system. The target is also more difficult to model since the exhaust plume will be an important part of the lander emissions. Our strategy is then to observe the low perilune orbit maneuver from a space-based sensor as described below, then pick up the lander from a ground-based Fisheye camera as described in the companion paper [13].

5.2 Seeing Craft on Ballistic sub-Orbital Trajectories

In §3 we discuss detecting objects on the ground and detecting their motion by trails in the regolith. Here we consider objects moving from place to place by hopping (impulsive mechanical) and flying (propulsive), without leaving trails between their locations. Hoppers and flyers were considered as well as the crewed rover in the Apollo [36] for surface mobility on the Moon, until now only rovers (or feet) have been used by the spacefaring powers on the Moon. Hoppers have the advantage over flyers in that they do not consume reaction mass and can recharge, but flyers have the advantage for long trips since the energy density of rocket fuel is greater than that of battery or mechanical energy storage system – very much like the tradeoff between internal combustion and electric vehicles on Earth and suggesting future studies of hybrid vehicles. China's Chang'e 7 mission to the South Pole will have a mini-hopping probe or flyer [37], so it is worth considering the detection of such vehicles, especially those hopping or flying from an illuminated crater rim into a PSR and back – a typical range of 5 to 30 km each way. Reference [35] Fig. 9 shows some interesting examples of Vertical Takeoff Vertical Landing (VTVL) trajectories which fly from one point on the lunar surface to another, avoiding lunar topography over a one degree/30 km range. A rough estimate from minimum energy flat-Moon dynamics, is that the vehicle will have an apoapsis altitude half the travel distance, or 2.5 to 15 km, and will be aloft for a minute or two. It is thus unlikely that such trips will be observed from an orbiting sensor or even a small constellation, given that this is only a few percent of an orbital period and observations would have to contend with lunar straylight. A better approach might be a HDR camera imaging the PSR from a site on the crater rim, or a Fisheye camera looking towards zenith [13].

In the long term, people and resources might be transported large distances from one place on the Moon to another via sub-orbital transport (SOT) vehicles. Fig. 5-1 shows some properties of lunar ballistic trajectories calculated from the equations in [38] Ch. 6 versus range angle, which corresponds to 30.3 km/degree at the lunar surface. It is conjectured but not proven here that the maximum altitude of a minimum energy trajectory occurs when the range angle is exactly 90° – that is, a quarter of the body circumference. This trip is shown in Table 5-1 in the “hemi” column. A single-stage LOX-LH₂ vehicle can transport just 15% of its mass on this trip. This is poor economics for transporting LOX-LH₂, but much better if only hydrogen is transported and the oxygen electrolytically extracted from local rocks since hydrogen is only 11% of the fuel reaction mass. Such journeys might also be worthwhile if the cargo is exceptionally valuable, a one-way hard landing for some missions is useful, or nuclear thermal propulsion (NTP) is used. Our worked example in STK below considers a 90°/2729 km trip from the South Pole on the rim of Shackleton Crater to a He-3 rich region in Oceanus Procellarum near the Equator [39]. Because of the payload reduction between hemispherical and antipodal trips, northern hemisphere locations would best be served by SOTs to and from the North pole. Trips longer than the “regional” trip in Table 5-1 would fall below the Fisheye FOV (extending from zenith to 30° above the horizon) except during the near-vertical liftoff/final approach, but these trips would be high enough (>50 km) with long enough TOF to be seen from orbit, except for near-antipodal ($\Psi > 171^\circ$) trajectories.

Table 5-1: Round-trip soft-landing mass budget for sub-orbital transport, LOX-LH₂ propellant

	regional	hemi	antipodal	
Range	1,728.0	2,728.5	5,426.6	km
Range Angle Ψ	57.0	90.0	179.0	deg
Fight path angle at surface γ	30.0	22.5	0.3	deg
Δv one-way	1340.1	1517.4	1667.1	m/s
Time of flight	47.9	52.4	54.1	min
Max altitude	298.5	359.7	7.5	km
Isp	440	440	440	s
Vehicle Dry Mass	15%	15%	15%	
Δv outbound, 10% margin	2,948	3,337	3,668	m/s
Payload	22%	15%	9%	
Mass at outbound landing	51%	47%	43%	
Mass at return launch	29%	32%	35%	
Δv return, 10% margin	2,948	3,337	3,668	m/s
Mass at return landing	15%	15%	15%	

It is interesting to note (“antipodal” column in Table 5-1) that fast, difficult-to-observe ballistic trajectories can be used on the Moon by using very low flight path angles just clearing the lunar topography (altitude above the geoid of ~10 km). This is not possible on Earth because of the atmosphere.

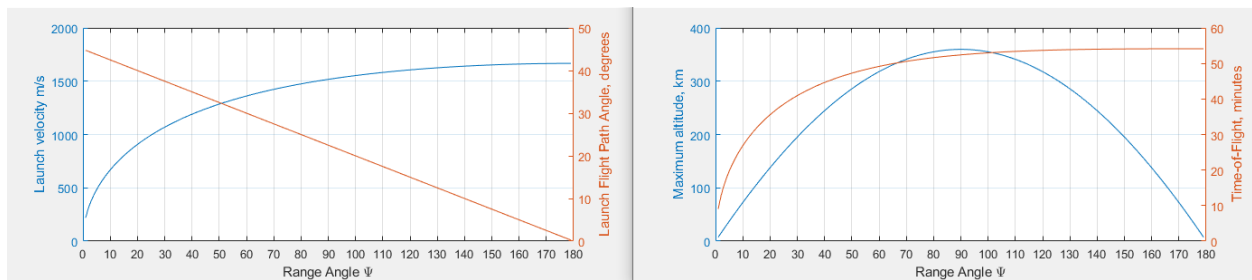


Fig. 5-1: Properties of Lunar Ballistic Trajectories

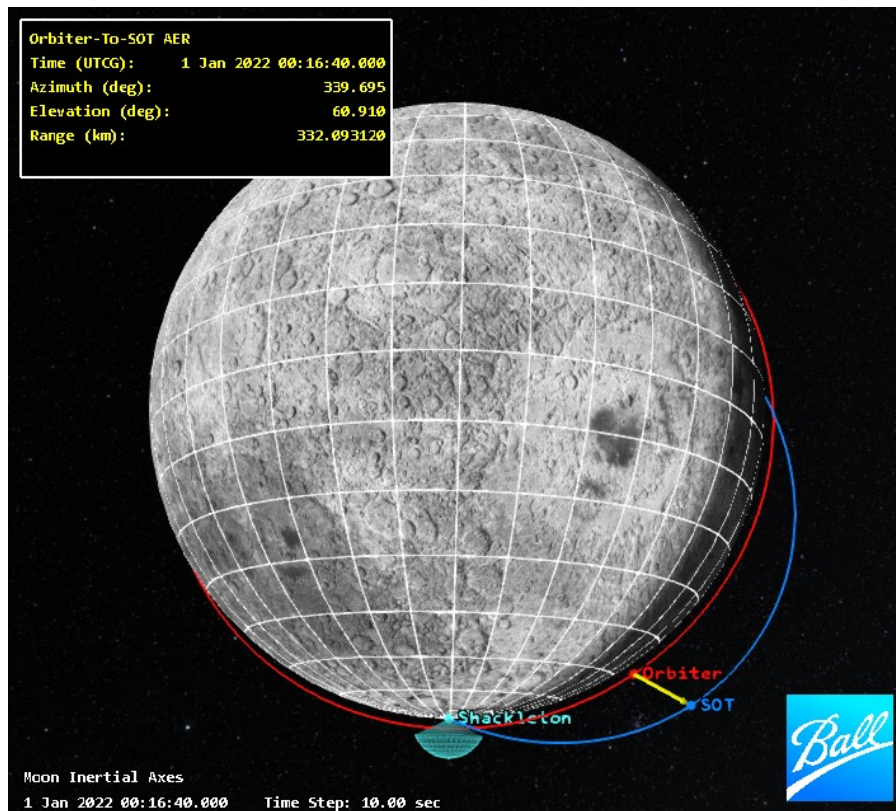


Fig. 5-2: Detection of a Sub-Orbital Transport by an Orbiting Sensor. The fisheye FOV [13] is cyan.

6 Bonus Science

The orbits and instrument suites described in this paper can serve understanding of these common anthropogenic and science phenomena:

Table 6-1: Correlation of Natural and Anthropogenic Observations

Anthropogenic phenomenon	Instruments	Measurement	Companion Science	Comment	Sample reference
Physical presence of lander, rover, impact crater, other	Vis imager Laser altimeter(?)	Object Detection & Identification	Topographic mapping	LRO resolution: 0.5 m (LROC NAC) 5.0 m (altimeter)	[40],[41], [2]
Landing plume blast zone: 1) particle smoothing	Vis imager	Reflectivity	Feldspar concentration	Blast zone typical reflectance increase: 10%	[42], [30], [43]
Landing plume blast zone: 2) regolith removal exposes denser material, rock	Thermal Infrared radiometric imager; also multispectral	Radiant emission, 8 to 12 um and multiband	Mineral composition, crater studies	thermal inertia increase and inhomogeneity (“blockiness”), excavated composition	[44], [45], [43]
Landing plume	Vis imager, Event camera	Visible flash	Meteor impact, addendum to seismic studies	2 cameras to discriminate cosmic ray events	[9]
Lander gas/volatile emission	Vis, SWIR imager and/or spectrometer	Reflectivity, spectral reflectivity	Surface volatiles, volatile origin		[30], [7]

Notes to Table:

Ref. [42]: These reflectance and backscattering character similarities suggest that reflectance changes resulting from rocket exhaust interacting with regolith during spacecraft landing have not significantly changed on the order of 40-50 years.

Ref. [44]: The data confirmed the presence of a large population of nighttime positive thermal anomalies or hot spots associated with the ejecta of small and large fresh impact craters (see Fig. 5). The accepted explanation for this phenomenon is that impacts excavate and expose blocky material with higher thermal inertia than the fine-grained lunar regolith.

Ref. [45]:

The formation of large lunar craters excavates numerous $\geq 1\text{m}$ ejecta fragments onto the Moon’s surface. These recently exposed rocks have high thermal inertia and remain warm during the lunar night relative to the surrounding lunar soils (called regolith), which have low thermal inertia.

7 Conclusions

The scientific community has pioneered surface imagery modeling with the SNR, FOV, GSD, and model fidelity required for SDA in visible light and, with the exception of GSD, for thermal IR. This capability needs to be expanded and operationalized so timely information on events on and near the Moon can be collected and reported in hours instead of weeks to months. The phenomenology also needs to be broadened to thermal IR at much smaller GSD, and to particle sensors for gas and dust.

Given the geometrical difficulty of persistent EOIR monitoring of sub-orbital trajectories (including landings and ascents), it may be worthwhile to consider orbiting “tripwire” sensors of gas and dust to indicate an unannounced propulsion event has occurred somewhere on the lunar surface.

The same sensor suite that enables comprehensive awareness of the lunar surface and near-lunar space can be used scientifically to detect flashes from meteor impacts [9, 10] and fresh craters [11, 12].

8 References

- [1] G. Chin, S. Brylow, M. Foote et al., Lunar Reconnaissance Orbiter Overview: The Instrument Suite and Mission, *Space Sci Rev* DOI 10.1007/s11214-007-9153-y, 2007
- [2] R. V. Wagner, D. M. Nelson, J. B. Plescia et al., Coordinates of Anthropogenic Features on the Moon, *Icarus*, 283:92-103, 2017
- [3] A. M. Lawitzke, J. Van Cleve, J. Contreras et al., Hybrid Sensor for Joint Space Domain Awareness and Lunar Surface Intelligence, *AMOS 2022*
- [4] A. P. Ingersoll, T. Svitek, and B. C. Murray, Stability of Polar Frosts in Spherical Bowl-Shaped Craters on the Moon, Mercury, and Mars, *Icarus*, 100:40-47, 1992
- [5] S. A. Cota, C. J. Florio, D. J. Duvall, and M. A. Leon, The Use of the General Image Quality Equation in the Design and Evaluation of Imaging Systems, *Proc SPIE* Vol. 7458, 74580H
- [6] W. M. Farrell, P. Prem, O. J. Tucker et al., A lingering local exosphere created by a gas plume of a lunar lander, *Icarus*, 376:114857
- [7] S.T. Shipley, P.T. Metzger, and J.E. Lane, Lunar Cold Trap Contamination by Landing Vehicles, *ASCE International Conference on Engineering, Science, Construction and Operations in Challenging Environments-Earth and Space*, 2014
- [8] P. T. Metzger, Dust Transport and Its Effects Due to Landing Spacecraft, *Lunar Dust Conference LPI No. 2141*, paper 5040
- [9] D. H. Needham, D. E. Moser, R. M. Suggs et al., Impact Flash Monitoring Facility on the Deep Space Gateway, *Deep Space Gateway Science Workshop 2018*, paper 3031, 2018
- [10] A. Liakos, A. Z. Bonanos, E. M. Xilouris et al., NELIOTA: Methods, statistics, and results for meteoroids impacting the Moon, *Astronomy & Astrophysics*, 633:A112, 2020
- [11] J. T. S. Cahill, D. H. Needham, R. Weber et al., Assessing the Present-Day Impact Flux to the Lunar Surface Via Impact Flash Monitoring and Its Implications for Sustained Lunar Exploration, *Planetary Science Decadal Survey White Paper*
- [12] E. J. Speyerer, R. Z. Povilaitis, M. S. Robinson et al., Quantifying Crater Production and Regolith Overtun on the Moon with Temporal Imaging, *Nature*, 538:215-218, 2016
- [13] J. E. Van Cleve, D. P. Osterman, A. M. Lawitzke et al., A Year in the Life of the Shackleton Space Domain Awareness Station, *AMOS 2022*
- [14] M. Klonowski, M. J. Holzinger, and N. O. Fahrner, Optimal Cislunar Architecture Design Using Monte Carlo Tree Search Methods, *AMOS 2022*
- [15] D. Folta and D. Quinn, Lunar Frozen Orbits, *AIAA/AAS Astrodynamics Specialist Conference and Exhibit, AIAA 2006-6749* <https://arc.aiaa.org/doi/10.2514/6.2006-6749>, 2012
- [16] D. Folta, Lunar Frozen Orbits, *NASA Technical Reports Server* <https://ntrs.nasa.gov/citations/20080041459>
- [17] S-Y. Park and J. L. Junkins, Orbital Mission Analysis for a Lunar Mapping Satellite, *AIAA-94-3717-CP*, DOI <https://arc.aiaa.org/doi/abs/10.2514/6.1994-3717>, 1994
- [18] J.-P. Williams, B. T. Greenhagen, D. A. Paige et al., Seasonal polar temperatures on the Moon, *J. Geophys. Res.*, 124:2505–2521, 2019
- [19] A. R. Vasavada, D. A. Paige, and S. E. Wood, Near-Surface Temperatures on Mercury and the Moon and the Stability of Polar Ice Deposits, *Icarus*, 141: 179-193, 1999
- [20] P.O. Hayne, J. L. Bandfield, M. A. Siegler et al., Global Regolith Thermophysical Properties of the Moon From the Diviner Lunar Radiometer Experiment, *JGR Planets*, 122:2371-2400, 2017
- [21] D. A. Glenar, T. J. Stubbs, E. W. Schwieterman et al., Earthshine as an illumination source at the Moon, *Icarus*, 321:841-856, 2019
- [22] J. Stopar, Lunar South Pole Radar Images and Earthshine Mode (85°S to Pole), Lunar and Planetary Institute Regional Planetary Image Facility, *LPI Contribution 2347*, <https://repository.hou.usra.edu/handle/20.500.11753/1488>
- [23] P. O. Hayne, O. Aharonson, and N. Schorghofer et al., Micro Cold Traps on the Moon, *Nature Astronomy*, 5:169-175, 2021
- [24] M. Robinson, Mystery Rocket Body Found!, <http://roc.sese.asu.edu/posts/1261>, 2022
- [25] K. Chang, They Found Two New Craters on the Moon and Discovered a New Mystery, *New York Times*, 6/27/2022
- [26] E. Mazarico, M. K. Barker, and J. B. Nicholas, Advanced illumination modeling for data analysis and calibration. Application to the Moon, *Space Research*, 62:3214-3228, 2018

- [27] R. N. Clegg, B. L. Joliff, M. S. Robinson et al., Effects of rocket exhaust on lunar soil reflectance properties, *Icarus*, 227:176-194, 2014
- [28] R. N. Clegg-Watkins, B. L. Joliff, A. Boyd et al., Photometric characterization of the Chang'e-3 landing site using LROC NAC images, *Icarus*, 273:84-95, 2016
- [29] P. Prem, D. M. Hurley, D. B. Goldstein, and P. L. Varghese, The Evolution of a Spacecraft-Generated Lunar Exosphere, *JGR Planets*, 125 <https://doi.org/10.1029/2020JE006464>, 2020
- [30] R. N. Watkins, P. T. Metzger, D. Eppler et al., Understanding Rocket Exhaust Effects in Polar Regions During Powered Descent on the Moon, *Science Definition Team for Artemis*, paper 2059, 2020
- [31] B. M. Jakosky, R. P. Lin, J. M. Grebowsky et al, The Mars Atmosphere and Volatile Evolution (MAVEN) Mission, *Space Science Reviews*, 195:3-48, 2015
- [32] P. R. Mahaffy, M. Benna, T. King et al., The Neutral Gas and Ion Mass Spectrometer on the Mars Atmosphere and Volatile Evolution Mission, *Space Science Reviews*, DOI 10.1007/s11214-014-0091-1, 2014
- [33] M. Horanyi, Z. Sternovsky, M. Lankton et al., The Lunar Dust Experiment (LDEX) Onboard the Lunar Atmosphere and Dust Environment Explorer (LADEE) Mission. *Space Sci Rev*, DOI 10.1007/s11214-014-0118-7, 2104
- [34] G. H. Heiken, D. T. Vaniman, and B. M. French, *Lunar Sourcebook* Ch. 7, 1991
- [35] H. Chu, L. Ma, K. Wang et al., Trajectory optimization for lunar soft landing with complex constraints, *Advances in Space Research*, 60:2060-2076, 2017
- [36] E. Swift, *Across the Airless Wilds: The Lunar Rover and the Triumph of the Final Moon Landings*, 2021
- [37] A. Jones, *Space News*, <https://spacenews.com/china-targets-permanently-shadowed-regions-at-lunar-south-pole>, 2022
- [38] R. R. Bate, D. D. Mueller, and J. E. White, *Fundamentals of Astrodynamics*, Dover Books, 1972
- [39] W. Fa and Y-Q Jin, Quantitative estimation of helium-3 spatial distribution in the lunar regolith layer, *Icarus*, 190:15-23, 1997
- [40] M.S. Robinson et al., Lunar Reconnaissance Orbiter Camera (LROC) Instrument Overview, *Space Science Reviews*, 150:81-124, 2010)
- [41] B. Wu, J. Guo, Y. Zhang et al., Integration of Chang'E-1 Imagery and Laser Altimeter Data for Precision Lunar Topographic Modeling, " *IEEE Transactions on Geoscience and Remote Sensing*, 49:4889-4903, 2011
- [42] R. Watkins Ph.D. thesis , Photometric Investigations of Lunar Landing Sites and Siliic Regions Using LRO Narrow Angle Camera Images, Washington University PhD. Chapter 2, Effects of Rocket Exhaust on Lunar Soil Reflectance Properties
- [43] Y. Wu and B. Hapke, Spectroscopic observations of the Moon at the lunar surface, *Earth and Planetary Sciences Letters*, 484:145-153 , 2018
- [44] D. A. Paige et al., The Lunar Reconnaissance Orbiter Diviner Lunar Radiometer Experiment, *Space Sci Rev*, 150: 125–160 , 2010
- [45] S. Mazroue et al., Earth and Moon impact flux increased at the end of the Paleozoic, *Science*, 363:253-257 , 2019